Monthly Notices of the ROYAL ASTRONOMICAL SOCIETY

MNRAS **545,** 1–15 (2026) https://doi.org/10.1093/mnras/staf2177
Advance Access publication 2025 December 9

OPTICAM reveals hints of cyclotron emission from the intermediate polar V709 Cas

Z. A. Irving [1]★ N. Castro Segura [2] D. Altamirano,[1] S. Scaringi [3,4] M. Veresvarska [3] F. Vincentelli,[5] D. de Martino,[4] D. A. H. Buckley,[6,7] A. Castro[8] and R. Michel[8]

[1]*School of Physics and Astronomy, University of Southampton, University Road, Southampton SO17 1BJ, UK*
[2]*Department of Physics, University of Warwick, Gibbet Hill Road, Coventry CV4 7AL, UK*
[3]*Department of Physics, Centre for Extragalactic Astronomy, Durham University, South Road, Durham DH1 3LE, UK*
[4]*INAF – Osservatorio Astronomico di Capodimonte, Salita Moiariello 16, I-80131 Napoli, Italy*
[5]*INAF – Istituto di Astrofisica e Planetologia Spaziali, Via del Fosso del Cavaliere 100, I-00133 Roma, Italy*
[6]*South African Astronomical Observatory, PO Box 9, Observatory 7935, Cape Town, South Africa*
[7]*Department of Astronomy, University of Cape Town, Private Bag X3, Rondebosch 7701, South Africa*
[8]*Instituto de Astronomía, Universidad Nacional Autónoma de México, Carretera Tijuana-Ensenada Km. 107, Ensenada 22860, México*

Accepted 2025 December 5. Received 2025 December 5; in original form 2025 October 3

ABSTRACT

Magnetic cataclysmic variables of the intermediate polar (IP) subclass display a wide range of variability across different wavelengths. In late 2024 October/early November, the IP V709 Cas was observed over 10 nights by the OPtical TIming CAMera at the San Pedro Mártir Observatory in simultaneous three-colour (g, r, and i, or z band) photometry. On two of these nights, V709 Cas was simultaneously observed by the *Neutron star Interior Composition ExploreR* X-ray telescope. A periodogram analysis of the optical g- and r-band light curves reveals no prominent features at the white dwarf (WD) spin, but prominent features at the spin-orbit beat. In contrast, the X-ray and near-infrared (near-IR) i- and z-band periodograms show prominent features at the spin, but not the spin-orbit beat. Optical beat and near-IR spin pulsations have been seen in the IP PQ Gem, with simultaneous circular polarization detected in the near-IR, indicating cyclotron origin. We therefore speculate that we are seeing cyclotron radiation from V709 Cas, possibly adding it to the small group of cyclotron-emitting IPs. Combining analytical approximations with our expectation for cyclotron harmonics in the near-IR, we suggest a WD magnetic field strength of 10 MG $< B <$ 40 MG.

Key words: accretion, accretion discs – stars: individual: V709 Cas – novae, cataclysmic variables – stars: magnetic fields.

1 INTRODUCTION

Cataclysmic variables (CVs) are binary systems comprised of a white dwarf (WD) primary and low-mass secondary (see e.g. B. Warner 1995). Roche lobe overflow leads to material from the secondary being accreted on to the primary, though how this material reaches the primary depends on its magnetic field strength. If the primary is strongly magnetic (i.e. $\gtrsim$ 10 MG), the spin of the primary may become synchronous with the orbit of the system, allowing material to be funnelled along accretion streams directly on to the magnetic poles of the WD. Such systems are referred to as polars. For more weakly magnetized primaries, the spin of the primary will generally be asynchronous with the orbit of the system, leaving space for an accretion disc to form. If the primary is moderately magnetic, the inner-edge of this accretion disc will be truncated at some radius above the WD surface (referred to as the magnetospheric radius). The primary's magnetic field then funnels material from the inner-edge of the accretion disc on to its magnetic poles. Such systems are referred to as intermediate polars (IPs; see J. Patterson 1994 for a review). Magnetically confined accretion on to a compact object produces a diverse range of observational characteristics across a wide range of wavelengths; in this regard, IPs are very similar to neutron star low-mass X-ray binaries (LMXBs; e.g. B. Warner 2004).

The presence of spin pulsations in the X-ray and optical emission of CVs are the primary observational characteristics of magnetism (e.g. B. Warner 1995). Polars get their name from the fact that their optical–near-infrared (near-IR) emission is usually dominated by circularly polarized cyclotron radiation; since the WD is rotating, this circular polarization is modulated on the WD's spin period. In IPs, cyclotron radiation is harder to detect due to their weaker magnetic fields (e.g. D. T. Wickramasinghe, K. Wu & L. Ferrario 1991a) and/or the accretion disc diluting polarized emission (e.g. V. Piirola, P. Hakala & G. V. Coyne 1993). However, circularly polarized emission has been found in $\sim$ 11 IPs (L. Ferrario, D. de Martino & B. T. Gänsicke 2015; S. B. Potter & D. A. H. Buckley 2018, and references therein), and it has been suggested that these 'polarized IPs' are low-field polar progenitors evolving towards synchronism (A. J. Norton, G. A. Wynn & R. V. Somerscales 2004).

★ E-mail: z.irving@soton.ac.uk

V709 Cassiopeiae (hereafter V709 Cas) is an IP that was discovered during the *ROSAT* all-sky survey. Follow-up pointed observations found that V709 Cas had a 'hard' X-ray spectrum (peaking at ~ 1 keV), and suggested a 312.8 s spin period (F. Haberl & C. Motch 1995). Shortly after its X-ray discovery, V709 Cas was optically identified and confirmed as a CV (C. Motch et al. 1996), and a few years later an orbital period of 5.340 ± 0.005 h was determined from spectroscopy (J. M. Bonnet-Bidaud et al. 2001). The WD mass is estimated to be $0.88^{+0.05}_{-0.04}$ $M_\odot$ (A. W. Shaw et al. 2018), and using the *Gaia* DR3 parallax of 1.35 ± 0.02 mas (Gaia Collaboration 2016; L. Lindegren et al. 2021; Gaia Collaboration 2023), the distance to V709 Cas is 725 ± 9 pc[1] (C. A. L. Bailer-Jones et al. 2021).

Like a number of other fast-rotating IPs (e.g. XY Ari; K. Koyama et al. 1991, PQ Gem; S. R. Rosen, J. P. D. Mittaz & P. J. Hakala 1993, DO Dra; A. J. Norton et al. 1999), the X-ray spin pulsations of V709 Cas are double-peaked (A. J. Norton et al. 1999; D. Martino et al. 2001; K. Mukai et al. 2015). In the optical, however, spin pulsations are not always seen. From 3000–7000 Å photometry, V. P. Kozhevnikov (2001) was able to see pulsations at the spin frequency, ω, and found that they were quasi-sinusoidal. V. P. Kozhevnikov (2001) also identified a 317.94 s periodicity that they attributed to the spin-orbit beat, $\omega - \Omega$, whose power was similar to that of the spin. Unlike the spin pulsations, V. P. Kozhevnikov (2001) found that the beat pulsations were double-peaked (and also showed considerable night-to-night variations). Later optical studies found that the spin pulsations of V709 Cas were either absent (e.g. F. Tamburini, D. de Martino & A. Bianchini 2009), or only recoverable on some nights (L. Hric et al. 2014).

In the most recent photometric study of V709 Cas, S. M. Rao et al. (2026) found spin and beat periods of 312.7478 ± 0.0002 and 317.9267 ± 0.0002 s, respectively, using data collected by the *Transiting Exoplanet Survey Satellite (TESS)*. The *TESS* bandpass covers red optical through near-IR wavelengths (6000–10 000 Å), possibly marking the return of V709 Cas's spin pulsations to the optical. By studying the relative powers of the spin and beat signals over time, S. M. Rao et al. (2026) found that while the spin is usually the dominant periodicity, there are epochs where the beat is dominant. To explain this, S. M. Rao et al. (2026) suggested that V709 Cas is a disc-overflow system that shows episodes of stream-fed accretion. Long-term variations in the accretion configuration have been invoked to explain similar behaviour in other IPs (e.g. FO Aqr; D. Martino et al. 1999), and may explain why the spin pulsations of V709 Cas 'disappeared' from the optical after the observations of V. P. Kozhevnikov (2001).

Herein, we present an analysis of multiband photometric data on V709 Cas obtained with the OPtical TIming CAMera (OPTICAM; A. Castro et al. 2019) mounted on the 2.1 m telescope at the San Pedro Mártir Observatory (OAN-SPM), in México. OPTICAM is equipped with three 2048×2048 s CMOS cameras and a set of SDSS filters (u or g, r, and i or z), allowing for simultaneous three-colour observations in the 3551–8932 Å central wavelength range. We also analyse simultaneous *Neutron star Interior Composition ExploreR* (*NICER*; K. C. Gendreau, Z. Arzoumanian & T. Okajima 2012) X-ray data. In Section 2, we detail the OPTICAM and *NICER* observations and reduction. In Section 3, we describe the analyses we performed. In Section 4, we present the results of these analyses. In Section 5, we interpret our results. Our final thoughts are then given in Section 6.

[1] https://dc.zah.uni-heidelberg.de/gedr3dist/q/cone/form

Table 1. OPTICAM observations.

Epoch	Date (YYYY-MM-DD)	Filters	Cadence (s)	Exposure (s)
1	2024-10-25	g, r, i	3	21 330
2	2024-10-26	g, r, i	3	14 718
3	2024-10-27	g, r, i	3	16 104
4	2024-10-28	g, r, i	3	15 507
5	2024-10-30	g, r, i	3	19 278
6	2024-10-31	g, r, z	3	19 827
7	2024-11-01	g, r, i	3	9885
8	2024-11-02	g, r, i	3	23 136
9	2024-11-03	g, r, i	3	4692
10	2024-11-04	g, r, i	3	10 503

2 DATA REDUCTION

2.1 OPTICAM

V709 Cas was observed on 10 nights from 2024 October 25 to 2024 November 4. These observations are listed in Table 1, including the filters used, the observing cadence, and the total exposure time. To reduce storage requirements, all observations were performed using the '2x2' binning mode, which reduces the image sizes from 2048x2048 to 1024x1024 (A. Castro et al. 2019, 2024).

For each image, cosmic rays were removed using the L.A.Cosmic algorithm (P. G. Dokkum 2001) as implemented in `AstroSCRAPPY` version 1.2.0 (C. McCully et al. 2018). Background images were estimated using the `SExtractorBackground` estimator from `photutils` version 1.13.0 (L. Bradley et al. 2024) with the `box_size` parameter set to 64 pixels. To identify sources, we used the `SourceFinder` routine from `photutils`, which combines source detection and deblending, to identify sources 5σ above the estimated background with the `npixels` parameter set to 32. Barycentric corrections were also applied to the time stamps of each image. Photometry was then performed on the background subtracted images using the optimal photometry algorithm described in T. Naylor (1998). To correct for atmospheric effects, we computed relative light curves using a bright unlisted comparison source nearby in the field. The coordinates of our comparison source were approximately RA 00:28:51, Dec. +59:17:26, and we found no evidence of intrinsic variability in our comparison source. The resulting light curves for each filter can be seen in Fig. 1.

2.2 *NICER*

In 2024, V709 Cas was observed four times by *NICER*. These observations are listed in Table 2; observations that were simultaneous with OPTICAM are marked with an asterisk. We note that the exposure times of the non-simultaneous observations are shorter than the spin period of V709 Cas (312.75 s), and so we do not include analysis of these observations.

NICER data were primarily reduced using `HEASOFT` version 6.35.1. We computed energy spectra using the `nicerl3-spect` tool with `bkgmodeltype = 3c50` (R. A. Remillard et al. 2022). `nicerl3-spect` performs the *NICER*-recommended analysis steps to compute the background, response, and spectra files. After applying Barycentric corrections to the photon arrival times with `barycorr`, we also extracted light curves using version 2.2.6 of the X-ray spectral timing Python package `stingray` (D. Huppenkothen et al. 2019; M. Bachetti et al. 2024). We compute 'soft' X-ray light curves in the 0.5–2.5 keV energy range (similar to the 0.1–

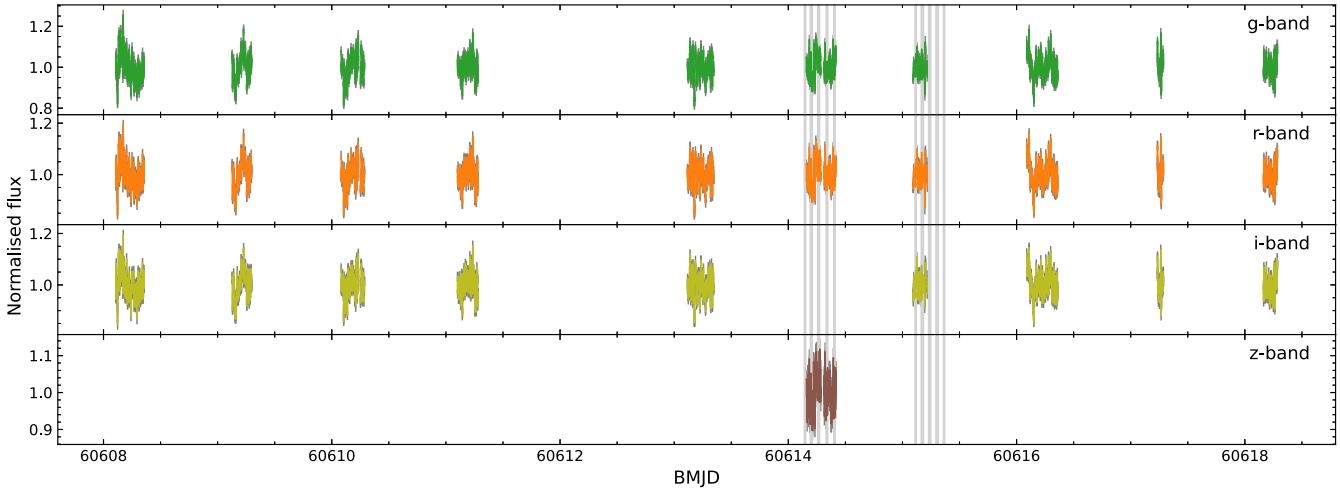

Figure 1. OPTICAM light curves of V709 Cas from Table 1 binned to a 1 min time resolution. The shaded regions represent the GTIs of the simultaneous *NICER* observations listed in Table 2.

Table 2. *NICER* observations of V709 Cas.

Date (YYYYMMDD)	ObsID	Exposure (s)
2024-10-31*	7204990101	6105
2024-11-01*	7204990102	6945
2024-11-21	7204990103	247
2024-11-23	7204990105	22

Note. Observations that are simultaneous with OPTICAM are marked with an asterisk.

2.4 keV energy range of the *ROSAT* pointed observations studied in F. Haberl & C. Motch 1995), and 'hard' light curves in the remaining 2.5–12 keV energy range. The Good Time Intervals (GTIs) of our extracted light curves are represented by the shaded grey regions in Fig. 1.

3 DATA ANALYSIS

3.1 Identification of periodic signals

To identify periodic signals, we use the Lomb–Scargle periodogram (LSP; N. R. Lomb 1976; J. D. Scargle 1982). We prefer the LSP to the classical periodogram in this case since the LSP does not require uniformly sampled input, allowing for an improved frequency resolution at the cost of potential aliasing and windowing effects (J. T. VanderPlas 2018). We compute the LSP using ASTROPY version 6.1.4 (Astropy Collaboration 2022).

3.2 Characterization of periodic signals

3.2.1 Frequency errors

To estimate the frequency errors on features identified in our LSPs, we use a Monte Carlo method. The first step is to re-sample the light curve with replacement, meaning that some points will not be re-sampled, while others will be re-sampled more than once. Therefore, this method effectively changes the 'weight' of each data point in the computation of the LSP. Additionally, this method also slightly changes the window function, allowing aliases to be rejected (e.g. D. R. Zurek et al. 2009). We then compute the LSP of the re-sampled light curve, fit a second-order polynomial to the tallest peak in the LSP, and use this polynomial to interpolate the frequency of maximum power. By repeating the above, we can construct frequency distributions for features in the original LSP; interpolating the frequency of maximum power prevents the frequency grid of the LSP from discretizing this distribution. We can then approximate the 68 per cent confidence interval on a given feature in the original LSP using the 16th and 84th percentiles of its frequency distribution.

3.2.2 Amplitudes

To characterize the amplitude of a signal, we use the peak-to-peak pulsed fraction as defined in L. Bildsten et al. (1997). We approximate the maximum and minimum pulsed flux using the relative extrema of the phase binned light curve. For brevity, we refer to the peak-to-peak pulsed fraction as simply the pulsed fraction.

3.3 Power-spectrum modelling

In addition to identifying periodic signals, we also seek to model the power spectrum of V709 Cas by fitting the averaged periodogram. To compute the averaged periodogram, we use `stingray`. Since OPTICAM observations are not perfectly uniformly sampled, we first re-bin our light curves to a time resolution of 5 s before computing averaged periodograms with a segment length of 3500 s. This resulted in 33 g-band segments, 34 r-band segments, 29 i-band segments, and just five z-band segments. We therefore exclude the z-band data from this analysis since there were too few segments to reliably model the power spectrum. For the periodogram normalization, we use the fractional RMS normalization such that integrating the averaged periodogram yields the square of the fractional RMS of the light curve.

3.3.1 Models

In this case we are only interested in modelling the broad-band noise, which we assume can be described by a zero-centred Lorentzian:

$$P(\nu) = A\frac{\nu_{\rm break}}{\nu_{\rm break}^2 + \nu^2}, \quad (1)$$

where ν is frequency, A is the normalization, and $\nu_{\rm break}$ is the break frequency. Zero-centred Lorentzians are commonly used to model the aperiodic X-ray variability of LMXBs (e.g. M. A. Nowak 2000; T. Belloni, D. Psaltis & M. van der Klis 2002), and M. Veresvarska et al. (2024) showed that they can equally be used to model the aperiodic optical/near-IR variability of IPs.

We explicitly note that the periodogram cannot account for Poisson noise, and so it is also necessary to model the white noise using a constant, c:

$$P(\nu) = c. \tag{2}$$

3.4 X-ray flux estimation

To estimate the X-ray flux of V709 Cas in absolute units (i.e. erg cm^{-2} s^{-1}), we jointly model our *NICER* spectra using `XSPEC` version 12.5.1 (K. A. Arnaud 1996). In jointly modelling these spectra, we assume that the spectral shape is the same. However, we allow the integrated flux to vary between observations by including a `constant` component that we fix to 1 for ObsID 7204990101, but leave as a free parameter for ObsID 7204990102.

Above 10 keV, the X-ray spectra of IPs are well described by cooling flow models such as `mkcflow` (R. F. Mushotzky & A. E. Szymkowiak 1988). Between 0.5 and 8 keV, however, the X-ray spectra of IPs are often too flat to be described by simple absorption and cooling flow models; instead, these spectra are better fit with a photon power law (e.g. K. Mukai et al. 2003). Despite being unphysical, a power law has a similar effect to convolving a cooling flow model with `pwab`, a power-law absorption model (e.g. K. Mukai et al. 2015; K. Mukai 2017). In our case, we note that *NICER* only covers the 0.2–12 keV energy range. As such, the differences between a phenomenological power law model and a more physical cooling flow model, in terms of both goodness of fit and inferred flux,[2] are likely to be minimal. We therefore choose to model the continuum emission of V709 Cas using the simpler `powerlaw` model, which we convolve with `TBabs` to represent absorption due to the interstellar medium. In CVs, some fraction of the emission may also be absorbed by material within the system. In `XSPEC`, partial covering absorption can be modelled using a `partcov` component, which we convolve with the `phabs` absorption model. Physically, `phabs` represents photoelectric absorption, and is considered to be the best absorption model for CVs (e.g. K. Mukai 2017).

In addition to their continuum emission, CVs often show discrete spectral features, such as the Fe K complex (e.g. K. Yoshida, H. Inoue & Y. Osaki 1992). Phenomenologically, these spectral features can be modelled using `gaussian` components. When fitting emission lines, it is common to fix the width (sigma parameter) to prevent the component from becoming too broad (for a recent example, see M. Kimura et al. 2025). In our case, we fix the emission line width to 0.1 keV, roughly matching *NICER*'s energy resolution. To verify the significance of emission line components, we use the F-test and adopt the conventional significance threshold of $p \leq 0.05$. The only exception to this is the Fe K complex, which we explicitly decompose into three Gaussians with line energies of 6.4 keV (fluorescence K_α), 6.67 keV (He-like), and 6.97 keV (H-like). Our starting model is therefore `constant*TBabs*(partcov*phabs)*(powerlaw + gaussian + gaussian + gaussian)`.

[2]Provided we do not extrapolate the model beyond *NICER*'s energy range.

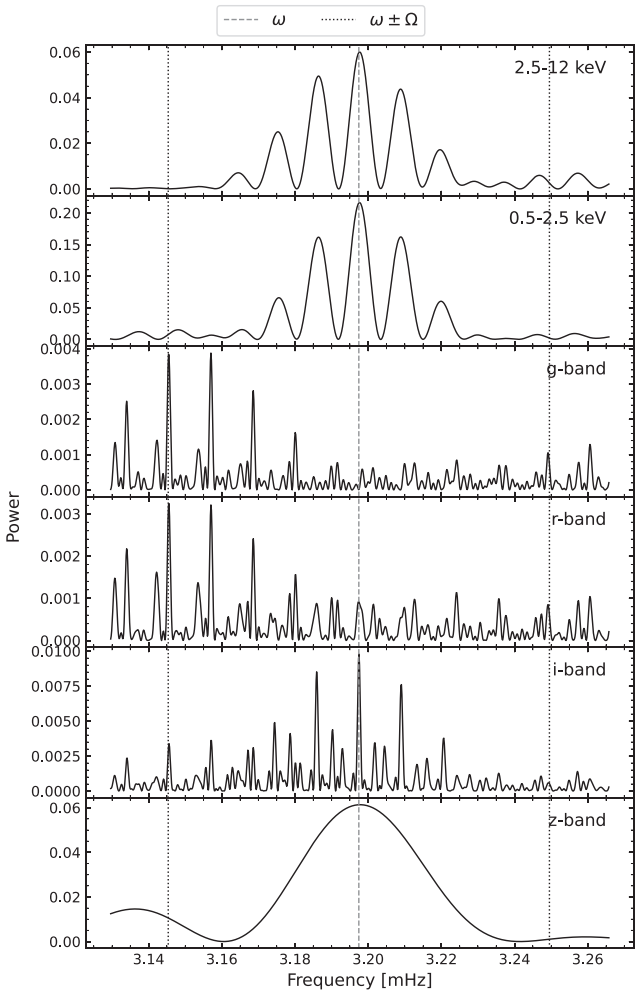

Figure 2. LSPs of the combined light curves from all nights for each band. The vertical lines show the spin frequency, ω (dashed line), and the beat frequency, $\omega - \Omega$ (dotted line).

4 RESULTS

4.1 Identification of periodic signals

4.1.1 *Fundamental frequencies*

To search for spin and beat pulsations in our light curves, we computed LSPs around the 312.75 s spin frequency reported by S. M. Rao et al. (2026). These LSPs are presented in Fig. 2, with vertical lines corresponding to the spin, ω (dashed line), and the spin-orbit side bands, $\omega \pm \Omega$ (dotted lines).

From Fig. 2, it can be seen that the LSPs of the hard and soft X-ray light curves, as well as those of the i- and z-band light curves, are dominated by the spin frequency (and aliases thereof). Conversely, the g- and r-band LSPs are dominated by the $\omega - \Omega$ beat frequency and corresponding aliases. A weak feature at $\omega - \Omega$ can also be seen in the i-band LSP, while the z-band LSP lacks the resolution required to identify a beat. The X-ray LSPs show no features at $\omega - \Omega$. No prominent features at the $\omega + \Omega$ side band can be seen in any of these periodograms.

Following the method described in Section 3.2.1, the X-ray LSPs from Fig. 2 suggest spin periods of 312.73 ± 0.03 s (hard) and 312.73 ± 0.01 s (soft), while the i-band LSP suggests a spin period

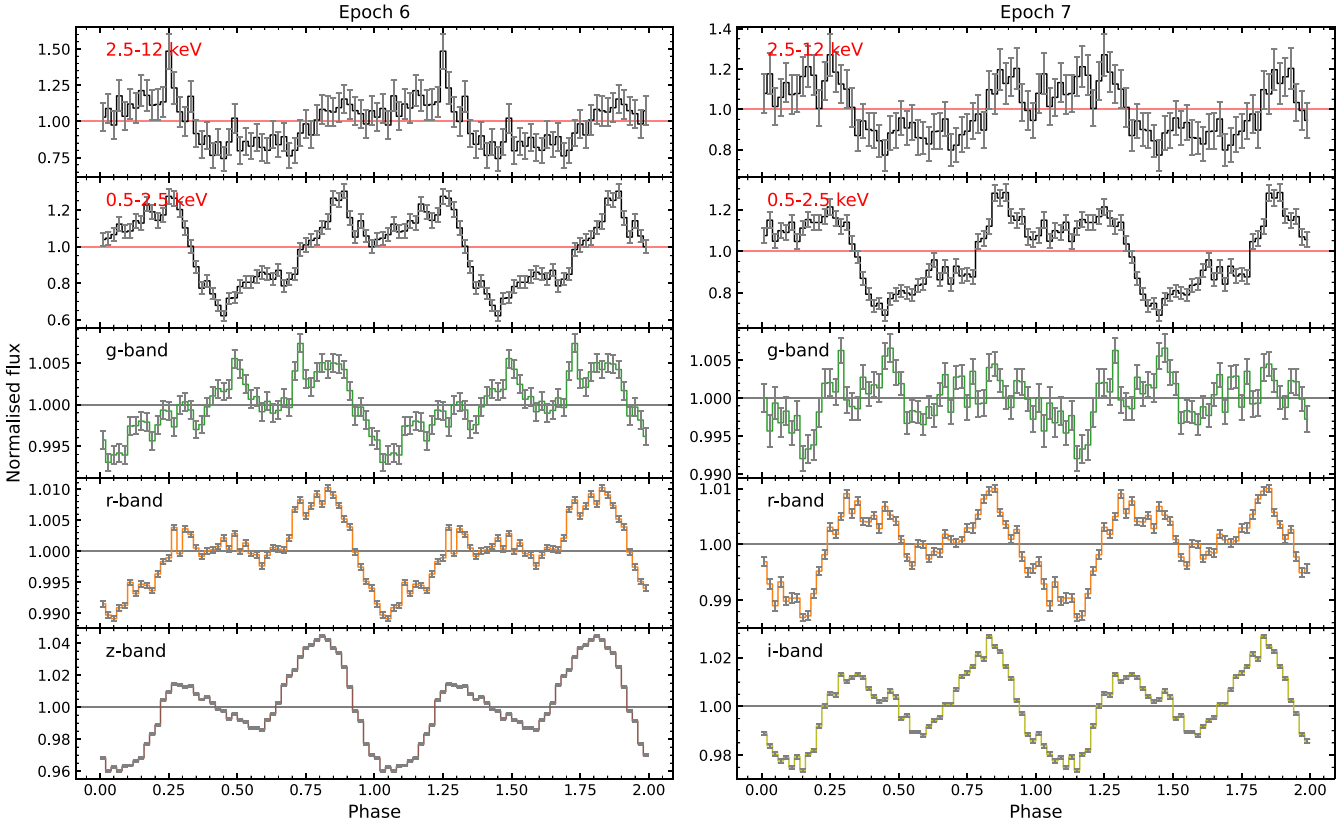

Figure 3. Light curves for Epochs 6 and 7 folded on the 312.73 s spin period. Two periods are presented for clarity.

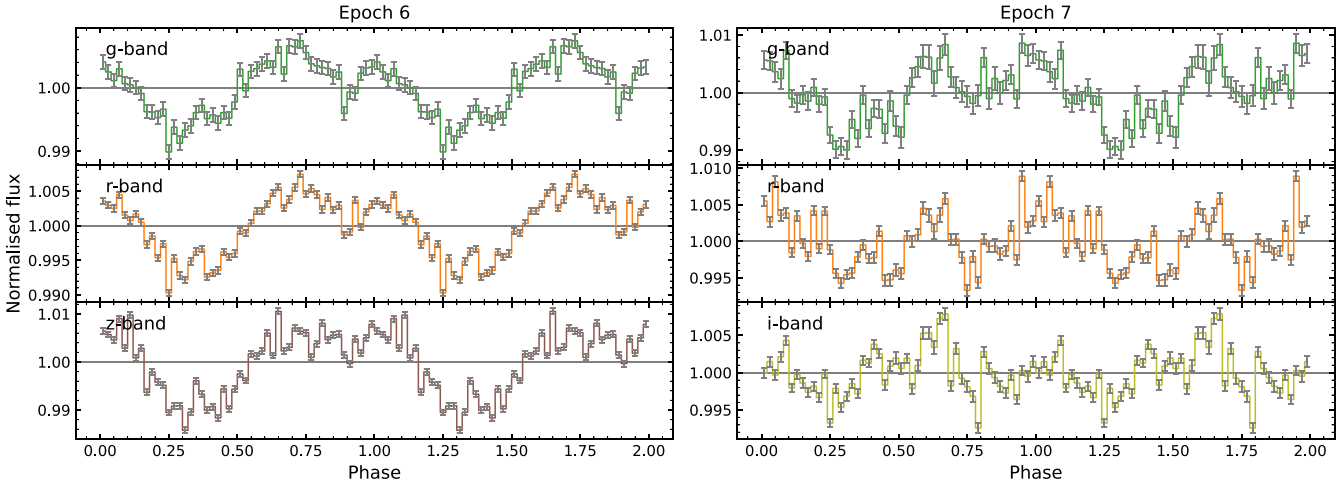

Figure 4. Light curves for Epochs 6 and 7 folded on the 317.91 s beat period. Two periods are presented for clarity.

of $312.748^{+0.004}_{-0.003}$ s.[3] Similarly, the *g*- and *r*-band LSPs suggest beat periods of $317.915^{+0.005}_{-0.007}$ and $317.913^{+0.006}_{-0.007}$ s, respectively. The *g*-band beat and *i*-band spin periods therefore imply an orbital period of $5.345^{+0.006}_{-0.008}$ h. All of these periods are consistent with previously reported values (Section 1).

To visualize the pulse profiles, we folded all of our light curves on the X-ray spin period of 312.73 s, and additionally folded our OPTICAM light curves on the *g*-band beat period 317.91 s. For all phase folds, we used an arbitrary time of zero phase of BMJD 60608. We note that we do not fold the X-ray light curves on the beat period since none of our X-ray LSPs show beat features. The spin-folded light curves for Epochs 6 and 7, for which we have simultaneous *NICER* data, are presented in Fig. 3, while the beat-folded OPTICAM light curves for these same epochs are presented in Fig. 4. The phase-folded light curves for the remaining epochs are presented in Appendix A.

As can be seen in Fig. 3, the spin-folded light curves change drastically from X-rays to near-IR. Within a given waveband, the spin

[3]We do not attempt to infer a spin period from the *z*-band LSP due to the poor resolution.

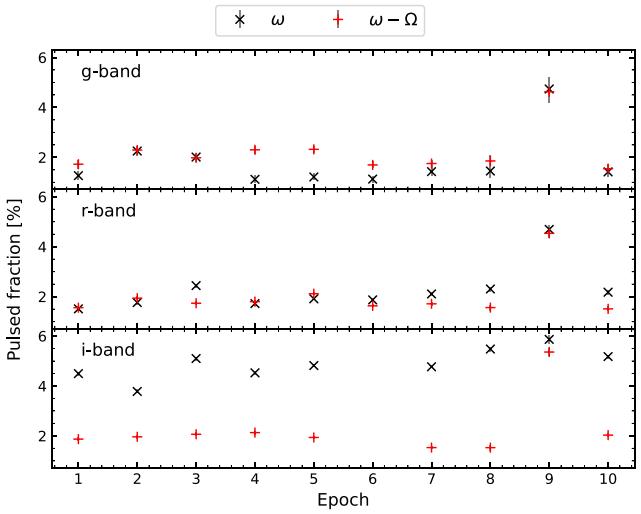

Figure 5. Spin (ω; black 'x' markers) and beat ($\omega - \Omega$; red '+' markers) pulsed fractions for the OPTICAM g, r, and i bands as a function of epoch number.

pulsations can also be seen to vary from night to night. Considering first the X-rays, the soft band reveals a double-peaked pulse profile consistent with those seen in A. J. Norton et al. (1999) and K. Mukai et al. (2015), while the increased scatter seen in the hard band makes the pulse profile difficult to characterize.

From the spin-folded OPTICAM light curves shown in Fig. 3, it can be seen that the the pulse profile becomes clearer with increasing wavelength: the g band shows a large amount of scatter, though pulsations are somewhat visible, while the z band shows clear double-peaked pulsations. The double-peaked OPTICAM pulsations appear asymmetrical, with one peak having a larger amplitude than the other, while in the X-rays both peaks can be seen to have similar amplitudes. It can also be seen that there are no appreciable phase lags between the different OPTICAM bands.

Regarding the beat pulsations shown in Fig. 4, it can be seen that the night-to-night variations are more drastic than in the case of the spin. In terms of shape, the beat pulsations can be either single- or double-peaked, depending on the night (Appendix A). Within a given epoch, the beat pulse profile appears similar across all bands, with the exception of Epoch 7, which shows a large amount of scatter. The qualitatively similar beat pulsations from optical to near-IR is in contrast to the strongly wavelength-dependent spin pulsations described above.

Aside from the above qualitative differences, the spin and beat pulsations also exhibit quantitative differences in amplitude over time and across wavelengths. To check for correlations between the spin and beat variability, we computed the nightly pulsed fractions of the spin and beat pulsations for the OPTICAM g, r, and i bands, for which we have multiple nights of data. The results of this are presented in Fig. 5. To then investigate the wavelength dependence of the spin and beat pulsations, we computed their averaged pulsed fractions over all epochs (listed in Table 3), and in Fig. 6 we present the averaged OPTICAM pulsed fractions as a function of filter wavelength.

As can be seen from Fig. 5, the spin and beat pulsed fractions of the g and r bands appear highly correlated over time, while the i band shows a less clear correlation. In particular, Epoch 9 shows a large increase in the beat pulsed fraction across all three bands. In the g and r bands, the increased beat pulsed fraction is coincident with

Table 3. Average spin and beat pulsed fractions over all epochs.

Band	Pulsed fraction (per cent)	
	Spin	Beat
2.5–12 keV	62 ± 10	
0.5–2.5 keV	64 ± 3	
g	1.80 ± 0.07	2.21 ± 0.07
r	2.25 ± 0.03	2.01 ± 0.03
i	4.89 ± 0.03	2.23 ± 0.03
z	8.41 ± 0.09	2.48 ± 0.09

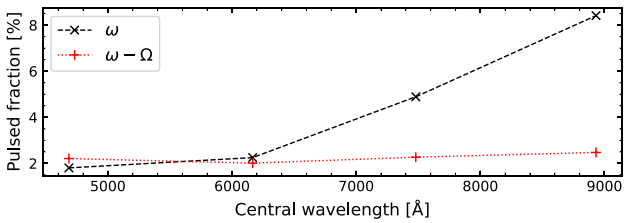

Figure 6. Average spin (ω; black dashed line) and beat ($\omega - \Omega$; red dotted line) pulsed fractions for the OPTICAM g, r, i, and z bands as a function of central wavelength.

a similarly large increase to the spin pulsed fraction. In the i band, however, the large increase to the beat pulsed fraction in Epoch 9 is coincident with a much smaller increase in the spin pulsed fraction.

Considering the averaged pulsed fractions listed in Table 3, it can be seen that the X-ray spin amplitude does not change significantly between our hard and soft bands. In both cases, the pulsed fraction is slightly in excess of 60 per cent, consistent with D. Martino et al. (2001). In contrast, it can be seen that the amplitude of the spin pulsations in the OPTICAM bands increases with increasing wavelength. In the optical g and r bands, the increase is relatively modest at ∼25 per cent. When moving from the optical to the near-IR, however, the i-band pulsed fraction is more than twice that of the r band; within the near-IR, the pulsed fraction increases by a further ∼72 per cent from the i to the z band.

Unlike the spin, the OPTICAM beat pulsed fractions list in Table 3 appear largely insensitive to wavelength: across all four bands, the beat pulsed fraction is ~ 2 per cent. As can be seen in Fig. 6, the optical spin and beat pulsations are therefore of similar amplitudes. In the near-IR, however, the i-band spin pulsed fraction is more than twice the beat pulsed fraction, and the z-band spin pulsed fraction is larger than the beat pulsed fraction by a factor > 3.

4.1.2 *Harmonic frequencies*

To search for spin and beat harmonics, we also computed LSPs around 2ω and $2(\omega \pm \Omega)$. These LSPs are presented in Fig. 7; in this case, the vertical lines correspond to the first harmonic of the spin, 2ω (dashed line), and the first harmonics of the spin-orbit side bands, $2(\omega \pm \Omega)$ (dotted lines). We recall that V. P. Kozhevnikov (2001) found peaks at $2(\omega - \Omega)$ but *not* 2ω.

As can be seen from Fig. 7, the higher frequency LSPs of all bands show their most prominent features at 2ω, in contrast to the findings of V. P. Kozhevnikov (2001). However, a feature at $2(\omega - \Omega)$ can be seen in the g-band LSP with slightly less power than that of the spin harmonic.

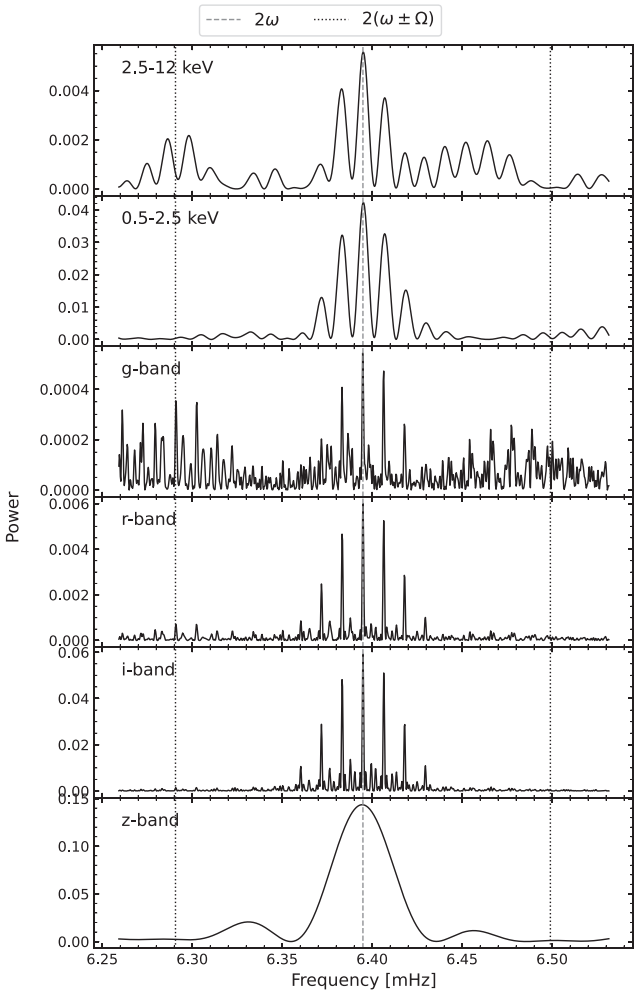

Figure 7. Similar to Fig. 2, but now vertical lines show the first harmonic of the spin, 2ω (dashed line), and the first harmonic of the beat frequency, $2(\omega - \Omega)$ (dotted line).

4.2 Power-spectrum modelling

The resulting fits from the OPTICAM power-spectrum modelling described in Section 3.3 are presented in Fig. 8.

As can be seen from Fig. 8, the broad-band variability of the g, r, and i bands are all well described by zero-centred Lorentzians. It can also be seen that both the r- and i-bands show a prominent signal at $\sim 2\omega$, while the i band also shows a weak feature at $\sim \omega$. In contrast, the averaged periodogram of the g-band light curve shows no prominent features at any frequency. From these fits, we find break frequencies of 0.66 ± 0.05, 0.68 ± 0.05, and 0.78 ± 0.06 mHz for the g, r, and i bands, respectively. These break frequencies show a slight, but not statistically significant, wavelength dependence. The average break frequency is 0.70 ± 0.03 mHz.

4.3 X-ray flux estimation

To estimate the X-ray flux, we jointly model our *NICER* spectra as described in Section 3.4. Our starting model, `constant*TBabs*(partcov*phabs)*(powerlaw + gaussian + gaussian + gaussian)`, resulted in a joint χ^2/dof of 553.00/329. The residuals of this fit revealed several

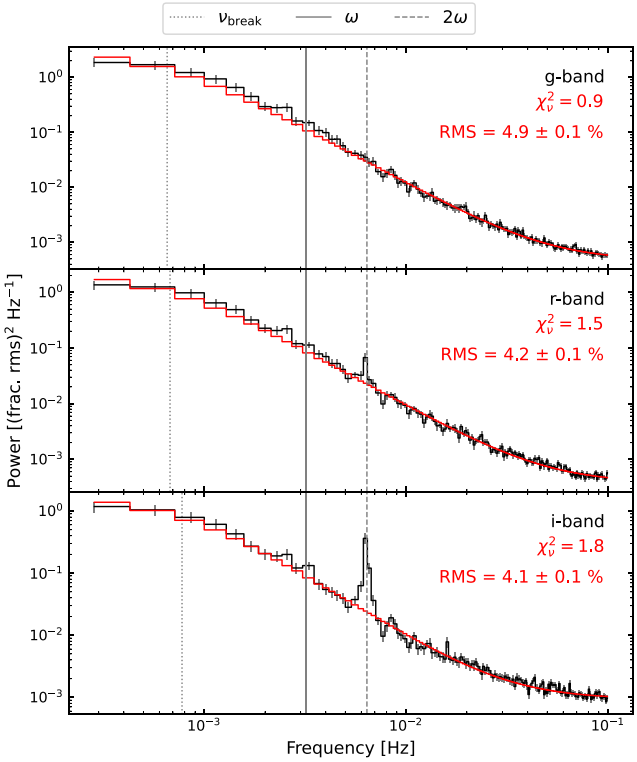

Figure 8. Zero-centred Lorentzian fits (red) to the averaged periodograms of our OPTICAM observations (black). The dotted vertical lines show the inferred break frequencies, while the solid and dashed vertical lines show the fundamental spin frequency of V709 Cas and its first harmonic, respectively.

excesses of emission at a range of energies, which we then modelled as emission lines. The first emission line we identified was at 0.558 ± 0.007 keV (χ^2/dof = 414.60/327; $p = 4 \times 10^{-21}$), possibly resulting from the 0.56 keV O VII line. We then identified a second emission line at 0.96 ± 0.02 keV (χ^2/dof = 388.19/325; $p = 2 \times 10^{-5}$), consistent with the 0.96 keV Fe XX line. We identified a third emission line at 10.00 ± 0.09 keV (χ^2/dof = 376.98/323; $p = 0.009$), most likely due to the 10.01 keV Ni XXVII line. We identified a final emission line at 1.80 ± 0.08 keV (χ^2/dof = 369.33/321; $p = 0.04$), consistent with the 1.86 keV Si XII line. The parameters of our final fit are listed in Table 4, while the resulting fits can be seen in Fig. 9.

From Fig. 9, it can be seen that our model yields $\chi^2_\nu < 1.5$ for both observations, indicating acceptable fits. That said, it can also be seen that there is a slight spectral change between these two observations, and so dedicated modelling of each observation may lead to better results. In particular, ObsID 7204990102 shows a hard component that is not seen in ObsID 7204990101. We note that a hard component has also been seen in previous X-ray studies of V709 Cas (e.g. K. Mukai et al. 2015; A. W. Shaw et al. 2018; D. Martino et al. 2020). However, since we are only interested in estimating the average X-ray flux, dedicated modelling of each observation is beyond the scope of this work.

Including a `cflux` term in the model presented in Table 4 yields an unabsorbed 0.5–12 keV flux for ObsID 7204990101 of $(6.12 \pm 0.08) \times 10^{-11}$ erg cm^{-2} s^{-1}. For ObsID 7204990102, the `constant` term indicates an 8.4 ± 0.7 per cent increase in flux: $(6.6 \pm 0.1) \times 10^{-11}$ erg cm^{-2} s^{-1}. The average flux over both

Table 4. Model parameters assuming the multicomponent model: `constant*TBabs*(powerlaw + gaussian + gaussian + gaussian + gaussian + gaussian)` fit to V709 Cas's *NICER* spectra.

Component	Parameter	Value
`constant`	factor	$1.084 \pm 0.007^{(a)}$
`TBabs`	nH (10^{22}cm^{-2})	0.078 ± 0.004
`partcov`	CvrFract	0.17 ± 0.05
`phabs`	nH (10^{22}cm^{-2})	$0.9^{+0.5}_{-0.3}$
`powerlaw`	PhoIndex	1.10 ± 0.03
	norm	$(3.9 \pm 0.2) \times 10^{-3}$
`gaussian`	LineE (keV)	0.558 ± 0.007
	Sigma (keV)	$0.1^{(b)}$
	norm	$(7.8^{+1.0}_{-0.8}) \times 10^{-4}$
`gaussian`	LineE (keV)	0.96 ± 0.02
	Sigma (keV)	$0.1^{(b)}$
	norm	$(1.4 \pm 0.3) \times 10^{-4}$
`gaussian`	LineE (keV)	1.80 ± 0.04
	Sigma (keV)	$0.1^{(b)}$
	norm	$(3 \pm 1) \times 10^{-5}$
`gaussian`	LineE (keV)	$6.4^{(b)}$
	Sigma (keV)	$0.1^{(b)}$
	norm	$(4 \pm 1) \times 10^{-5}$
`gaussian`	LineE (keV)	$6.67^{(b)}$
	Sigma (keV)	$0.1^{(b)}$
	norm	$(4 \pm 1) \times 10^{-5}$
`gaussian`	LineE (keV)	$6.97^{(b)}$
	Sigma (keV)	$0.1^{(b)}$
	norm	$(2 \pm 1) \times 10^{-5}$
`gaussian`	LineE (keV)	10.00 ± 0.09
	Sigma (keV)	$0.1^{(b)}$
	norm	$(1.2 \pm 0.6) \times 10^{-4}$

Note. [(a)] normalization factor for ObsID 7204990102 relative to ObsID 7204990101. [(b)] fixed. Errors represent the 1σ confidence interval.

observations is $(6.37 \pm 0.07) \times 10^{-11}$ erg cm^{-2} s^{-1}, suggesting an average X-ray luminosity of $(4.01 \pm 0.08) \times 10^{33}$ erg s^{-1}.[4]

5 DISCUSSION

5.1 Wavelength-dependent pulsations

In Section 4.1, we found that the spin pulsations of V709 Cas are highly sensitive to wavelength. In this section, we attempt to provide a physical explanation for this phenomenon.

5.1.1 The wavelength dependence of ω and $\omega - \Omega$

As mentioned in Section 1, S. M. Rao et al. (2026) found that the relative prominence of $\omega - \Omega$ and ω features in their LSPs would vary with time. We recall that S. M. Rao et al. (2026) therefore suggested that V709 Cas is a disc-overflow system that accretes primarily via a disc (when ω is most prominent), but also shows episodes of stream-fed accretion (when $\omega - \Omega$ is most prominent). We also recall that the *TESS* bandpass covers 6000–10 000 Å, meaning it partially overlaps with our *r* and *z* bands, while completely overlapping with the *i* band. Since we see ω and $\omega - \Omega$ simultaneously at different wavelengths within the *TESS* bandpass, the two signals being produced by different accretion mechanisms is difficult to reconcile. Indeed, periodicities at $\omega - \Omega$ can be produced

[4]Using a distance of 725 ± 9 pc (Section 1).

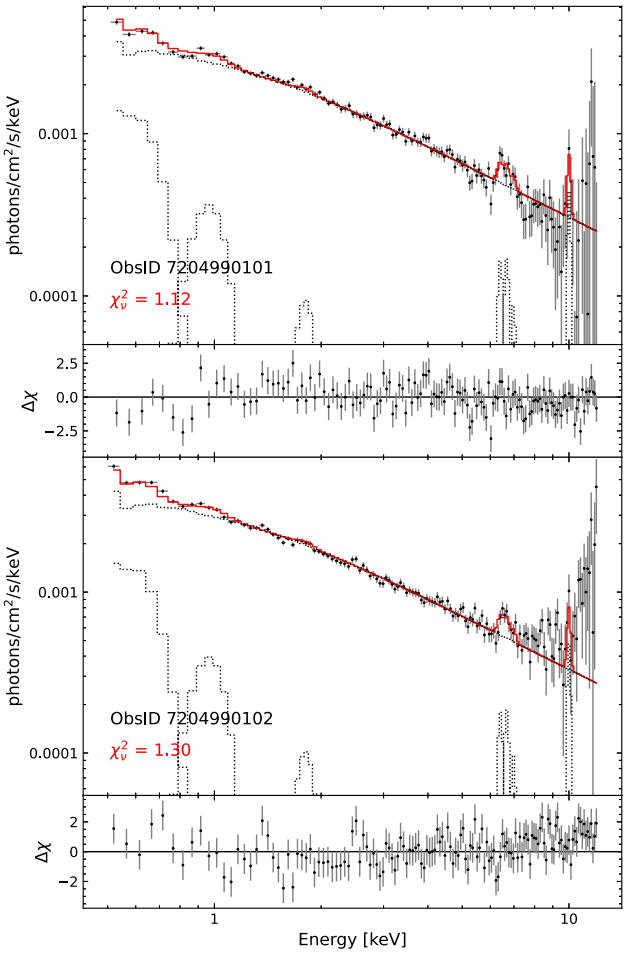

Figure 9. The fits to V709 Cas's unfolded *NICER* spectra reported in Table 4.

in disc-accreting systems if emission from the accretion column is reprocessed by material fixed in the orbital frame. Such reprocessing could take place, for example, where material from the secondary meets the outer edge of the accretion disc (B. J. M. Hassall et al. 1981), or in the atmosphere of the secondary (J. Patterson & C. M. Price 1981). As an example, A. E. Covington et al. (2022) noted that the IP RX J2133.7+5107 showed a period of enhanced accretion that was coincident with an increase in power of the $\omega - \Omega$ beat frequency. A. E. Covington et al. (2022) argued that disc-overflow was unlikely since the overflow stream could not be close to the inner-edge of the disc given the low $P_{\rm spin}/P_{\rm orb}$ ratio (≈ 0.022); instead, they invoked the reprocessing mechanism described above. In our case, V709 Cas has an even lower $P_{\rm spin}/P_{\rm orb}$ ratio of ≈ 0.016, leading us to also conclude that disc-overflow is unlikely. We therefore suggest that the optical $\omega - \Omega$ beat pulsations seen in Fig. 2 are produced by the reprocessing of soft X-rays in a disc-accreting system (e.g. G. A. Wynn & A. R. King 1992). One question that remains, however, is why the spin pulsations 'reappear' in the near-IR.

5.1.2 Hints of cyclotron emission?

The increasing spin pulsed fraction with increasing wavelength shown in Table 3 and Fig. 6 may be a result of cyclotron emission. To date, cyclotron emission has been confirmed in only 11 IPs: BG CMi (S. C. West, G. Berriman & G. D. Schmidt 1987; G. Chanmugam et al. 1990), PQ Gem (V. Piirola et al. 1993; S. R.

Rosen et al. 1993; S. B. Potter et al. 1997), RX J1712.6–2414 (D. A. H. Buckley et al. 1995), V2306 Cyg (M. Uslenghi et al. 2001), RX J2133.7+5107 (S. Katajainen et al. 2007), V405 Aur (V. Piirola et al. 2008), V3731 Oph (O. W. Butters et al. 2009), NY Lup and UU Col (S. Katajainen et al. 2010), IGR J15094-6649 (S. B. Potter et al. 2012), and IGR J17014-4306 (S. B. Potter & D. A. H. Buckley 2018). The most direct detection of cyclotron emission comes from circular polarization. Additionally, cyclotron humps, characteristic humps in a source's spectrum at harmonics of the fundamental cyclotron frequency, are another indication of cyclotron emission. Cyclotron humps can also be used to constrain the WD magnetic field strength (as in, for example, C. Littlefield et al. 2023), though such features are yet to be found in IPs (V. S. Dhillon et al. 1997).

From the photometric data we have on V709 Cas, we cannot straightforwardly determine the emission mechanism. However, we can make comparisons to systems in which cyclotron emission has been confirmed, and we find striking similarities between V709 Cas and PQ Gem. V. Piirola et al. (1993) found that R- and I-band light curves of PQ Gem showed pulsations at the 13.9 min WD spin period, while the U-, B-, and V-band light curves all showed pulsations at a 14.5 min period that they attributed to the spin-orbit beat (implying an orbital period of ~ 5 h). These findings were also supported by S. R. Rosen et al. (1993). V. Piirola et al. (1993) also found circular polarization in the R and I bands, with the I-band polarization variation being approximately twice that of the R band. As such, V. Piirola et al. (1993) concluded that the R- and I-band spin pulsations were a result of cyclotron emission. Given the similarities between our findings and those of V. Piirola et al. (1993) and S. R. Rosen et al. (1993), we find it likely that V709 Cas also emits cyclotron radiation.

Cyclotron emission can further explain the weak correlation between the i-band spin and beat pulsed fractions seen in Fig. 5. Following our suggestion in Section 5.1.1 that the beat pulsations are a result of reprocessed emission from the accretion column, an increase in the beat pulsed fraction implies an increase in the mass accretion rate (as in, for example, A. E. Covington et al. 2022). By extension, the low-amplitude g- and r-band spin pulsations are also likely to be a result of thermal emission given how tightly correlated their amplitudes are with the beat pulsed fraction. In contrast, the weak correlation between the i-band spin and beat pulsed fractions seen in Fig. 5 suggests that non-thermal emission (i.e. cyclotron radiation) contributes significantly to the i-band spin pulsations.

5.2 Double-peaked spin pulsations

As mentioned in Section 1, double-peaked spin pulsations are commonly observed in IPs, particularly those with shorter rotation periods. In Section 4.1 we showed that, in addition to the double-peaked X-ray spin pulsations previously reported in A. J. Norton et al. (1999), D. Martino et al. (2001), and K. Mukai et al. (2015), V709 Cas also shows double-peaked spin pulsations in the optical and near-IR.

Since X-rays are emitted from the accretion column (K. Aizu 1973; A. C. Fabian, J. E. Pringle & M. J. Rees 1976), double-peaked X-ray spin pulsations are often attributed to both poles being seen each rotation (e.g. A. J. Norton et al. 1999). S. R. Rosen et al. (1993) considered that the double-peaked R- and I-band spin pulsations of PQ Gem may be caused by emission from both poles, but also suggested that cyclotron beaming may be important. Since cyclotron radiation is emitted perpendicular to the magnetic field lines, cyclotron beaming would produce a flux minimum when the magnetic pole is pointed at the observer, while maxima would be produced when the magnetic pole subtends an angle of $\pm 90^{\circ}$ to the observer's line of sight, thereby producing two maxima per rotation from a single pole. From Fig. 3, however, it can be seen that the i- and z-band spin pulsations do not produce minima at the X-ray maxima. Therefore, if V709 Cas emits cyclotron radiation, cyclotron beaming must be unimportant; indeed, this is also the case for the prototypical polar AM Her, which shows double-peaked optical and near-IR spin pulsations whose maxima coincide with those of its X-ray spin pulsations (D. T. Wickramasinghe et al. 1991b). We therefore conclude that the double-peaked spin pulsations produced by V709 Cas are likely a result of both poles contributing to the observed flux.

5.2.1 *Asymmetries and night-to-night variations*

In their two-pole model of AM Her, D. T. Wickramasinghe et al. (1991b) showed that the relative flux contributions of each pole change with time, producing asymmetric double-peaked spin pulsations due to moving emission regions. Similarly, the variations in the asymmetry of V709 Cas's spin pulsations may also be a result of the varying visibilities of two emission regions. We also note that variations in the spin pulsations are a common feature of IPs (e.g. D. O'Donoghue, C. Koen & D. Kilkenny 1996; T. W. Reimer et al. 2008), and so night-to-night variations (as shown in Fig. 5) are not surprising.

5.3 Magnetic field strength

Using the power-spectrum models from Section 4.2, in addition to the inferred X-ray luminosity from Section 4.3, we can obtain a rough estimate of the surface magnetic field strength, B, of V709 Cas. Assuming a dipole field, we can rewrite equation 6.18 of J. Frank, A. King & D. J. Raine (2002) to yield

$$B_{30} = \frac{\dot{M}_{16}^{1/2} M_{*}^{1/4}}{R_{*,\mathrm{cm}}^{3}} \left[\frac{R_{\mathrm{M,cm}}}{5.1 \times 10^{8} \Lambda}\right]^{7/4}, \tag{3}$$

where B_{30} is the surface magnetic field strength in units of 10^{30} G, $\dot{M}_{16}$ is the mass accretion rate in units of 10^{16} g s^{-1}, M_{*} is the WD mass in solar masses, $R_{*,\mathrm{cm}}$ is the WD radius in cm, $R_{\mathrm{M,cm}}$ is the magnetospheric radius in cm, and Λ is a dimensionless quantity related to the accretion geometry. The accretion geometry determines how the Alfvén radius, R_{A} (R. F. Elsner & F. K. Lamb 1977) relates to the magnetospheric radius:

$$R_{\mathrm{A}} = \frac{R_{\mathrm{M}}}{\Lambda}.$$

For magnetized neutron stars, it is convention to assume $\Lambda \approx 0.5$ following P. Ghosh & F. K. Lamb (1979a,b), and so we also adopt this value. To solve equation (3), we therefore need to estimate the WD radius, magnetospheric radius, and mass accretion rate.

The WD radius can be approximated using the WD mass–radius relation of M. Nauenberg (1972). For a 0.88 $\mathrm{M}_{\odot}$ WD (A. W. Shaw et al. 2018), this relation gives a radius of 6.4×10^{8} cm.

We can interpret the average break frequency of 0.70 mHz found in Section 4.2 as the viscous frequency of the accretion disc at the magnetospheric radius (e.g. Y. E. Lyubarskii 1997; P. Arévalo & P. Uttley 2006; S. Scaringi 2014). Relating the viscous frequency to a Keplerian orbital radius yields 1.8×10^{10} cm; since the viscous frequency cannot be larger than the dynamical frequency (N. I. Shakura & R. A. Sunyaev 1973), this represents a *lower limit* on the magnetospheric radius.

The mass accretion rate, $\dot{M}$, can inferred by rearranging equation 1.5 of J. Frank et al. (2002) to yield

$$\dot{M} = \frac{L_{\rm acc} R_*}{G M_*}, \tag{4}$$

where $L_{\rm acc}$ is the accretion luminosity and G is the gravitational constant. It is difficult to measure $L_{\rm acc}$ directly since it will span a wide range of wavelengths. However, we can assign a *lower limit* to $L_{\rm acc}$ using X-ray luminosity found in Section 4.3, which implies $\dot{M} \gtrsim 2.2 \times 10^{16}$ g s^{-1}.

The values derived above suggest a magnetic field strength of $\gtrsim 10$ MG, which is considerably larger than the 1.9 ± 0.03 MG magnetic field strength estimated by V. F. Suleimanov, V. Doroshenko & K. Werner (2019). However, V. F. Suleimanov et al. (2019) were unable measure a break frequency for V709 Cas, and therefore estimated the magnetospheric radius using the co-rotation radius. For a spin period of 312.73 s, the co-rotation radius is 6.6×10^9 cm, which is a factor ~ 2.7 lower than our *lower limit* on $R_{\rm M}$. Correcting the magnetic field strength estimate of V. F. Suleimanov et al. (2019) by a factor $2.7^{7/4} \approx 5.9$ gives $B = 11.0 \pm 0.2$ MG, in agreement with our estimate.

5.3.1 Cyclotron harmonics

With a lower limit on the magnetic field strength, we can check that it is consistent with our suggestion of cyclotron emission by calculating the fundamental cyclotron frequency, $f_{\rm cyc}$, from equation 6.30 of J. Frank et al. (2002):

$$f_{\rm cyc} = \frac{eB}{2\pi m_e c}, \tag{5}$$

where e is the charge of an electron, B is the magnetic field strength, m_e is the electron mass, and c is the speed of light in a vacuum. It should be noted, however, that the fundamental cyclotron frequency (and low harmonics thereof) are believed to be obscured by the emitting material, such that only higher harmonics contribute significantly to the observed flux (e.g. J. Frank et al. 2002, chapter 6).

Following our interpretation that the i- and z-band spin pulsations found in Section 4.1 are a result of cyclotron emission, this implies cyclotron harmonics close to the central wavelengths of these filters (7480 and 8932 Å, respectively). The i and z bands roughly correspond to the 13th and 11th harmonics of a 10 MG field, fifth and sixth harmonics of a 20 MG field, and third and fourth harmonics of a 30 MG field, respectively. For a 40 MG field, second and third harmonics would be produced at $\sim$ 8900 and 6700 Å, respectively, and so would likely not be seen in the i band. Moreover, since it is generally the third to sixth harmonics that are seen (e.g. C. Littlefield et al. 2023), we find a 10 MG field unlikely. We therefore suggest that V709 Cas's magnetic field strength is in the 10 MG $< B <$ 40 MG range.

We note that our inferred magnetic field strength is more consistent with the expected field strength for a polar than an IP (e.g. B. Warner 1995). However, similarly large estimates have been made for other IPs. For example, V. Burwitz et al. (1996) estimated a field strength of 10–30 MG for UU Col, H. Vaeth, G. Chanmugam & J. Frank (1996) estimated a field strength of 9–21 MG for PQ Gem, and V. Piirola et al. (2008) estimated a field strength of 31.5 ± 0.8 MG for V405 Aur, all of which are known to emit cyclotron radiation. As such, we do not consider our result to be unphysical.

5.3.2 A polar progenitor?

Given the inferred magnetic field strength of 10 MG $< B <$ 40 MG, it is plausible that V709 Cas may evolve into a polar (as predicted by, e.g. G. Chanmugam & A. Ray 1984; A. R. King, J. Frank & H. Ritter 1985). Using numerical simulations, A. J. Norton et al. (2004) suggested that magnetic CVs with magnetic moments, μ, greater than $\sim 5 \times 10^{33}$ G cm^3 and orbital periods greater than 3 h will evolve into polars. Assuming a dipole field, and using the WD radius estimated in Section 5.3 (M. Nauenberg 1972), we find 2.6×10^{33} G cm^3 $< \mu < 1.0 \times 10^{34}$ G cm^3. Our estimations are therefore consistent with V709 Cas being a polar progenitor.

6 CONCLUSIONS

From 10 nights of OPTICAM observations on V709 Cas, we found spin and beat periods of $312.748^{+0.004}_{-0.003}$ and $317.915^{+0.005}_{-0.007}$ s, respectively. These periods are consistent with previous measurements (e.g. F. Haberl & C. Motch 1995; V. P. Kozhevnikov 2001; S. M. Rao et al. 2026). We also found that the spin pulsations of V709 Cas appear strongly wavelength dependent. In the optical regime, ω is not prominent in the LSP and instead prominent features are seen at the $\omega - \Omega$ beat frequency. In the near-IR, however, the opposite is true: ω is prominent, while $\omega - \Omega$ is not. Quantitatively, we showed that the pulsed fraction of the spin pulsations increases from 1.80 ± 0.07 per cent in the g band to 8.41 ± 0.09 per cent in the z band. In contrast, we showed that beat pulsations are much less sensitive to wavelength, increasing in pulsed fraction from 2.21 ± 0.07 per cent in the g band to just 2.48 ± 0.09 per cent in the z band. Based on similarities to PQ Gem (V. Piirola et al. 1993; S. R. Rosen et al. 1993), we argue that V709 Cas likely emits cyclotron radiation. If confirmed, V709 Cas would increase the number of cyclotron-emitting IPs to 12 (L. Ferrario et al. 2015; S. B. Potter & D. A. H. Buckley 2018, and references therein). In Section 5.3, we estimated the magnetic field strength to be in the 10 MG $< B <$ 40 MG range based on analytical approximations (Y. E. Lyubarskii 1997; J. Frank et al. 2002; P. Arévalo & P. Uttley 2006; S. Scaringi 2014) and our expectation for cyclotron humps in the i and z bands. This range is similar to the 9–21 MG magnetic field strength estimated for PQ Gem (H. Vaeth et al. 1996), which is not surprising given the similarities between these two systems.

To follow up this work, we suggest searching for circular polarization in the (near-)IR emission of V709 Cas. POLIMA 2, a polarimeter at the OAN-SPM, could be used to search for circular polarization in the I band, which partially overlaps with our i and z bands. Alternatively, the bandpass of the PEPSI spectropolarimeter at the Large Binocular Telescope (K. G. Strassmeier et al. 2015, 2018) also overlaps with our i and z bands. A benefit of PEPSI is that its high spectral resolution may allow circularly polarized wavelengths (i.e. cyclotron humps) to be identified. Therefore, in addition to testing for cyclotron emission, PEPSI may help to further constrain V709 Cas's magnetic field strength.

ACKNOWLEDGEMENTS

This research was based upon observations carried out at the OAN-SPM, Baja California, México. We thank the daytime and night support staff at the OAN-SPM for facilitating and helping obtain our observations. We acknowledge the specific contributions of Iván Zavala, Enrique Colorado, Edgar Cadena, and Félix Díaz, for the technical maintenance of OPTICAM. This research also made use of data obtained from the High Energy Astrophysics Science Archive

Research Center (HEASARC), a service of the Astrophysics Science Division at NASA/GSFC and of the Smithsonian Astrophysical Observatory's High Energy Astrophysics Division.

The authors acknowledge the use of the MATPLOTLIB (J. D. Hunter 2007), NUMPY (C. R. Harris et al. 2020), and SCIPY (P. Virtanen et al. 2020) software, which were instrumental in this work.

ZAI gratefully acknowledges support from the UK Research and Innovation's Science and Technology Facilities Council (STFC) grant ST/X508767/1. AC acknowledges support from the Royal Society Newton International Fellowships NF170803 and AL\221034. FMV has been supported by the European Union's Horizon Europe research and innovation programme through the Marie Skłodowska-Curie grant agreement No. 101149685, and acknowledges support from the Agencia Estatal de Investigación del Ministerio de Ciencia, Innovación y Universidades (AEI-MCIU) under grant PID2020-114822GB-I00 and PID2023-151588NB-I00.

We thank the referee for helpful suggestions that have improved the paper.

DATA AVAILABILITY

NICER ObsIDs 7204990101 and 7204990102 are publicly available on HEASARC.[5] The OPTICAM data analysed here can be made available (either as raw data or reduced data products) upon request. We note that a public reduction pipeline for OPTICAM is currently in development.

REFERENCES

Aizu K., 1973, Progr. Theor. Phys., 49, 1184
Arévalo P., Uttley P., 2006, MNRAS, 367, 801
Arnaud K. A., 1996, in Jacoby G. H., Barnes J. eds, ASP Conf. Ser. Vol. 101, Astronomical Data Analysis Software and Systems V. Astron. Soc. Pac., San Francisco, p. 17
Astropy Collaboration, 2022, ApJ, 935, 167
Bachetti M. et al., 2024, J. Open Source Softw., 9, 7389
Bailer-Jones C. A. L., Rybizki J., Fouesneau M., Demleitner M., Andrae R., 2021, AJ, 161, 147
Belloni T., Psaltis D., van der Klis M., 2002, ApJ, 572, 392
Bildsten L. et al., 1997, ApJS, 113, 367
Bonnet-Bidaud J. M., Mouchet M., de Martino D., Matt G., Motch C., 2001, A&A, 374, 1003
Bradley L. et al., 2024, astropy/photutils: 1.13.0, Zenodo, https://doi.org/10.5281/zenodo.12585239
Buckley D. A. H., Sekiguchi K., Motch C., O'Donoghue D., Chen A.-L., Schwarzenberg-Czerny A., Pietsch W., Harrop-Allin M. K., 1995, MNRAS, 275, 1028
Burwitz V., Reinsch K., Beuermann K., Thomas H. C., 1996, A&A, 310, L25
Butters O. W., Katajainen S., Norton A. J., Lehto H. J., Piirola V., 2009, A&A, 496, 891
Castro A. et al., 2019, Rev. Mex. Astron. Astrofis., 55, 363
Castro A. et al., 2024, Astron. Comput., 46, 100773
Chanmugam G., Frank J., King A. R., Lasota J. P., 1990, ApJ, 350, L13
Chanmugam G., Ray A., 1984, ApJ, 285, 252
Covington A. E. et al., 2022, ApJ, 928, 164
de Martino D. et al., 2001, A&A, 377, 499
de Martino D., Bernardini F., Mukai K., Falanga M., Masetti N., 2020, Adv. Space Res., 66, 1209
de Martino D., Silvotti R., Buckley D. A. H., Gänsicke B. T., Mouchet M., Mukai K., Rosen S. R., 1999, A&A, 350, 517
Dhillon V. S., Marsh T. R., Duck S. R., Rosen S. R., 1997, MNRAS, 285, 95
Elsner R. F., Lamb F. K., 1977, ApJ, 215, 897
Fabian A. C., Pringle J. E., Rees M. J., 1976, MNRAS, 175, 43
Ferrario L., de Martino D., Gänsicke B. T., 2015, Space Sci. Rev., 191, 111
Frank J., King A., Raine D. J., 2002, Accretion Power in Astrophysics, 3rd edn. Cambridge Univ. Press, Cambridge
Gaia Collaboration, 2016, A&A, 595, A1
Gaia Collaboration, 2023, A&A, 674, A1
Gendreau K. C., Arzoumanian Z., Okajima T., 2012, in Takahashi T., Murray S. S., den Herder J.-W. A. eds, Proc. SPIE Conf. Ser. Vol. 8443, Space Telescopes and Instrumentation 2012: Ultraviolet to Gamma Ray. SPIE, Bellingham, p. 844313
Ghosh P., Lamb F. K., 1979a, ApJ, 232, 259
Ghosh P., Lamb F. K., 1979b, ApJ, 234, 296
Haberl F., Motch C., 1995, A&A, 297, L37
Harris C. R. et al., 2020, Nature, 585, 357
Hassall B. J. M. et al., 1981, MNRAS, 197, 275
Hric L., Breus V., Katysheva N. A., Shugarov S. Y., Dubovský P., 2014, Astron. Nachr., 335, 362
Hunter J. D., 2007, Comput. Sci. Eng., 9, 90
Huppenkothen D. et al., 2019, ApJ, 881, 39
Katajainen S., Butters O. W., Norton A. J., Lehto H. J., Piirola V., 2007, A&A, 475, 1011
Katajainen S., Butters O., Norton A. J., Lehto H. J., Piirola V., Berdyugin A., 2010, ApJ, 724, 165
Kimura M. et al., 2025, ApJ, 985, 240
King A. R., Frank J., Ritter H., 1985, MNRAS, 213, 181
Koyama K. et al., 1991, ApJ, 377, 240
Kozhevnikov V. P., 2001, A&A, 366, 891
Lindegren L. et al., 2021, A&A, 649, A2
Littlefield C. et al., 2023, ApJ, 943, L24
Lomb N. R., 1976, Ap&SS, 39, 447
Lyubarskii Y. E., 1997, MNRAS, 292, 679
McCully C. et al., 2018, astropy/astroscrappy: v1.0.5 Zenodo Release, Zenodo
Motch C., Haberl F., Guillout P., Pakull M., Reinsch K., Krautter J., 1996, A&A, 307, 459
Mukai K., 2017, PASP, 129, 062001
Mukai K., Kinkhabwala A., Peterson J. R., Kahn S. M., Paerels F., 2003, ApJ, 586, L77
Mukai K., Rana V., Bernardini F., de Martino D., 2015, ApJ, 807, L30
Mushotzky R. F., Szymkowiak A. E., 1988, Fabian A. C., ed., Einstein Observatory Solid State Detector Observations of Cooling Flows in Clusters of Galaxies, Cooling Flows in Clusters and Galaxies. Vol. 229, Springer Netherlands, p. 53
Nauenberg M., 1972, ApJ, 175, 417
Naylor T., 1998, MNRAS, 296, 339
Norton A. J., Beardmore A. P., Allan A., Hellier C., 1999, A&A, 347, 203
Norton A. J., Wynn G. A., Somerscales R. V., 2004, ApJ, 614, 349
Nowak M. A., 2000, MNRAS, 318, 361
O'Donoghue D., Koen C., Kilkenny D., 1996, MNRAS, 278, 1075
Patterson J., 1994, PASP, 106, 209
Patterson J., Price C. M., 1981, ApJ, 243, L83
Piirola V., Hakala P., Coyne G. V., 1993, ApJ, 410, L107
Piirola V., Vornanen T., Berdyugin A., Coyne G. V., J. S., 2008, ApJ, 684, 558
Potter S. B., Buckley D. A. H., 2018, MNRAS, 473, 4692
Potter S. B., Cropper M., Mason K. O., Hough J. H., Bailey J. A., 1997, MNRAS, 285, 82
Potter S. B., Romero-Colmenero E., Kotze M., Zietsman E., Butters O. W., Pekeur N., Buckley D. A. H., 2012, MNRAS, 420, 2596
Rao S. M., Pandey J. C., Rawat N., Joshi A., Singh A. K., 2026, New Astron., 122, 102481
Reimer T. W., Welsh W. F., Mukai K., Ringwald F. A., 2008, ApJ, 678, 376
Remillard R. A. et al., 2022, AJ, 163, 130
Rosen S. R., Mittaz J. P. D., Hakala P. J., 1993, MNRAS, 264, 171
Scargle J. D., 1982, ApJ, 263, 835
Scaringi S., 2014, MNRAS, 438, 1233
Shakura N. I., Sunyaev R. A., 1973, A&A, 24, 337

[5] https://heasarc.gsfc.nasa.gov

Shaw A. W., Heinke C. O., Mukai K., Sivakoff G. R., Tomsick J. A., Rana V., 2018, MNRAS, 476, 554
Strassmeier K. G. et al., 2015, Astron. Nachr., 336, 324
Strassmeier K. G. et al., 2018, in Evans C. J., Simard L., Takami H. eds, Proc. SPIE Conf. Ser. Vol. 10702, Ground-Based and Airborne Instrumentation for Astronomy VII. SPIE, Bellingham, p. 1070212
Suleimanov V. F., Doroshenko V., Werner K., 2019, MNRAS, 482, 3622
Tamburini F., de Martino D., Bianchini A., 2009, A&A, 502, 1
Uslenghi M., Tommasi L., Treves A., Piirola V., Reig P., 2001, A&A, 372, L1
Vaeth H., Chanmugam G., Frank J., 1996, ApJ, 457, 407
van Dokkum P. G., 2001, PASP, 113, 1420
VanderPlas J. T., 2018, ApJS, 236, 16
Veresvarska M. et al., 2024, MNRAS, 534, 3087
Virtanen P. et al., 2020, Nat. Methods, 17, 261
Warner B., 1995, Cataclysmic Variable Stars. Vol. 28, Cambridge Univ. Press, Cambridge
Warner B., 2004, PASP, 116, 115
West S. C., Berriman G., Schmidt G. D., 1987, ApJ, 322, L35
Wickramasinghe D. T., Bailey J., Meggitt S. M. A., Ferrario L., Hough J., Tuohy I. R., 1991b, MNRAS, 251, 28
Wickramasinghe D. T., Wu K., Ferrario L., 1991a, MNRAS, 249, 460
Wynn G. A., King A. R., 1992, MNRAS, 255, 83
Yoshida K., Inoue H., Osaki Y., 1992, PASJ, 44, 537
Zurek D. R., Knigge C., Maccarone T. J., Dieball A., Long K. S., 2009, ApJ, 699, 1113

APPENDIX A: PHASE-FOLDED LIGHT CURVES

In this section we provide the phase-folded light curves for all epochs, excluding those already presented in Section 4.1, to more clearly demonstrate the qualitative wavelength-dependences and night-to-night variations. The light curves of Epochs 1 and 2, 3 and 4, 5 and 8, and 9 and 10 folded on the 312.73 s spin period found in Section 4.1 are presented in Figs A1, A2, A3, and A4, respectively.

As can be seen from Figs A1, A2, A3, and A4, the g-band light curves sometimes show spin pulsations consistent with those seen in the i band, while other times they do not. In particular, if the i-band spin pulsations are asymmetric, it is often the case that only the larger peak is shown in the g band. The r band, in contrast, almost always shows spin pulsations consistent with those seen in the i band, though sometimes with different relative peak heights. For example, Fig. A1 shows the r-band light curves having a large peak at phase ~ 0.2 and a smaller peak at phase ~ 0.75; in contrast, the i-band light curves either show a larger peak at phase ~ 0.75 (Epoch 1; left panel) or have similarly sized peaks (Epoch 2; right panel).

In Figs A5, A6, A7, and A8 we present the light curves of Epochs 1 and 2, 3 and 4, 5 and 8, and 9 and 10, respectively, folded on the 317.91 s beat period found in Section 4.1.

As can be seen from Figs A5, A6, A7, and A8, the beat pulsations are qualitatively similar in all bands within a given epoch. Generally, the beat pulsations appear single peaked, in contrast to the findings of V. P. Kozhevnikov (2001), though Epoch 3 (left panel of Fig. A6) shows double-peaked beat pulsations. It can also be seen that the beat pulsations show larger night-to-night variations than the spin pulsations.

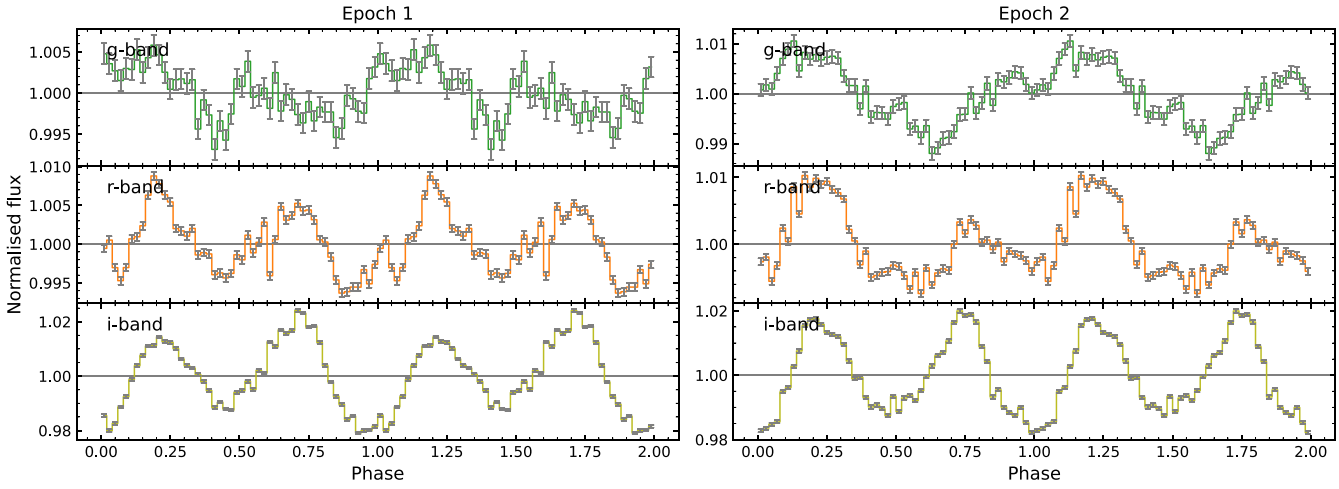

Figure A1. Light curves for Epochs 1 and 2 folded on the 312.73 s spin period.

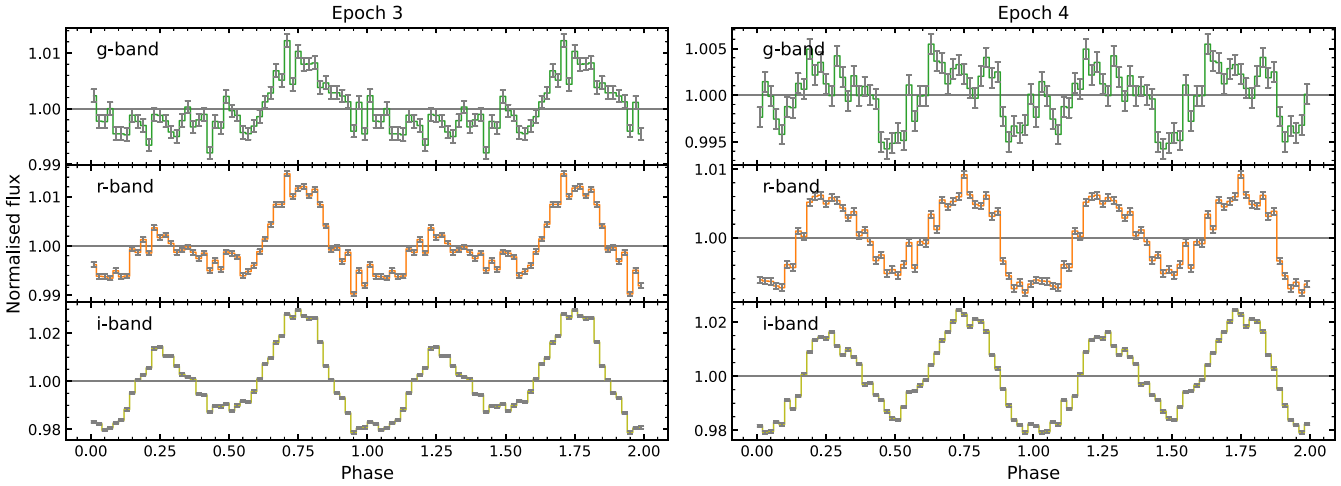

Figure A2. Light curves for Epochs 3 and 4 folded on the 312.73 s spin period.

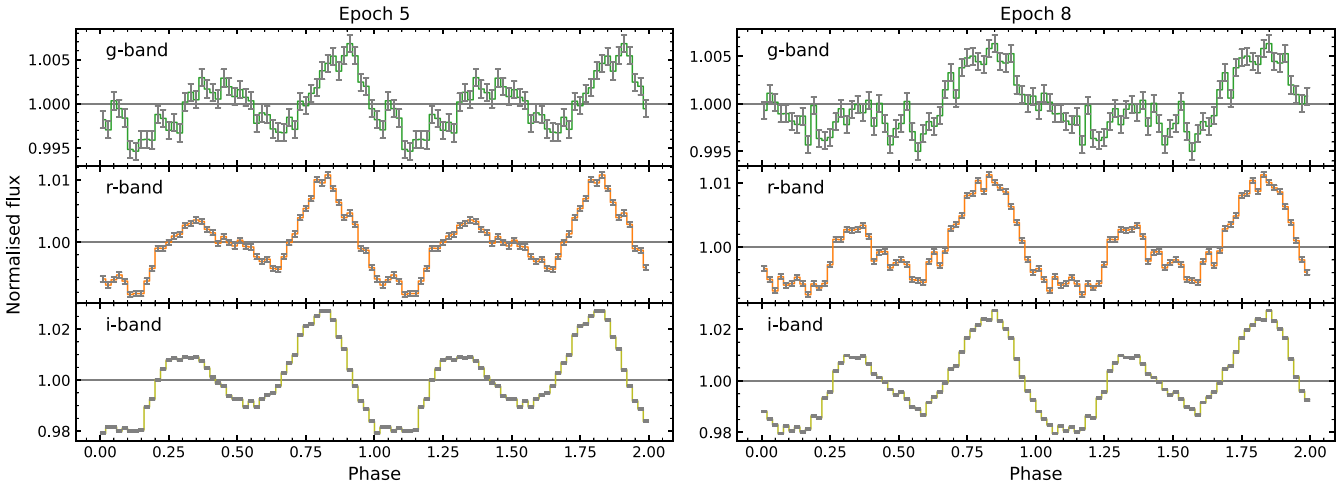

Figure A3. Light curves for Epochs 5 and 8 folded on the 312.73 s spin period.

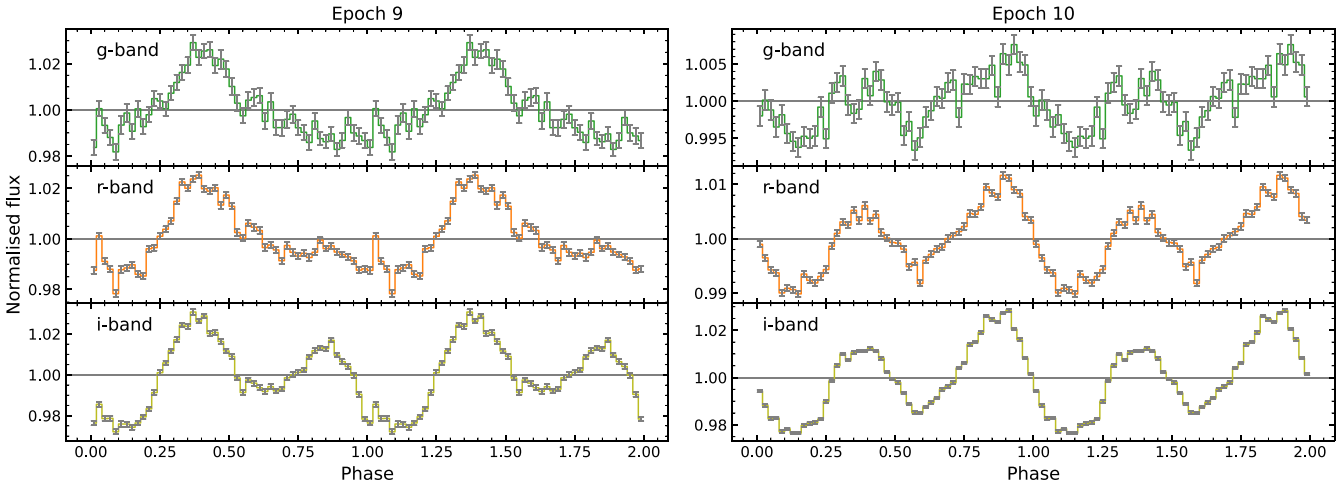

Figure A4. Light curves for Epochs 9 and 10 folded on the 312.73 s spin period.

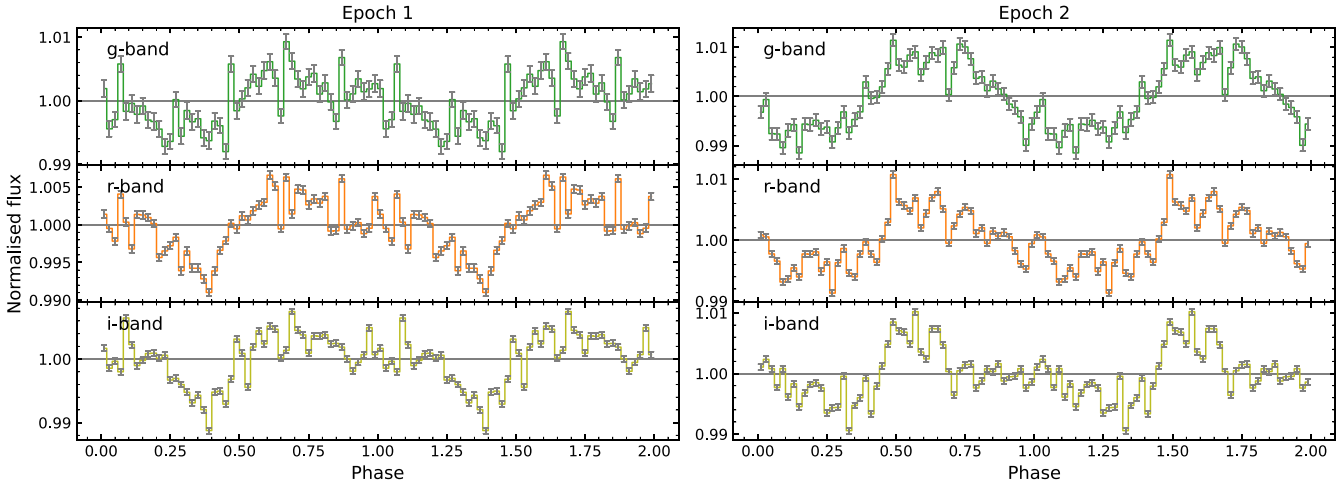

Figure A5. Light curves for Epochs 1 and 2 folded on the 317.91 s beat period.

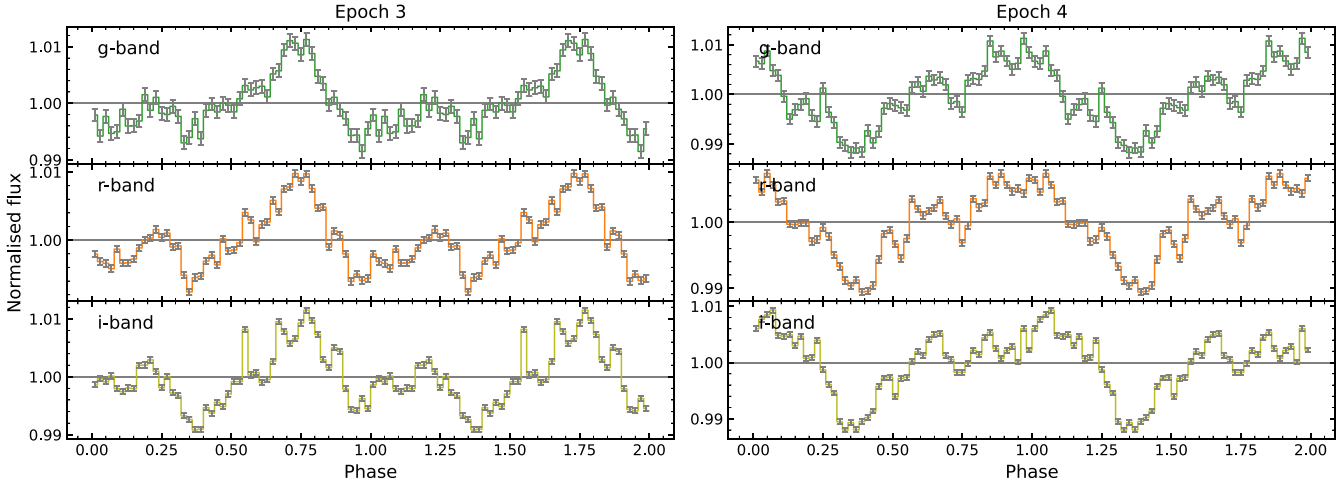

Figure A6. Light curves for Epochs 3 and 4 folded on the 317.91 s beat period.

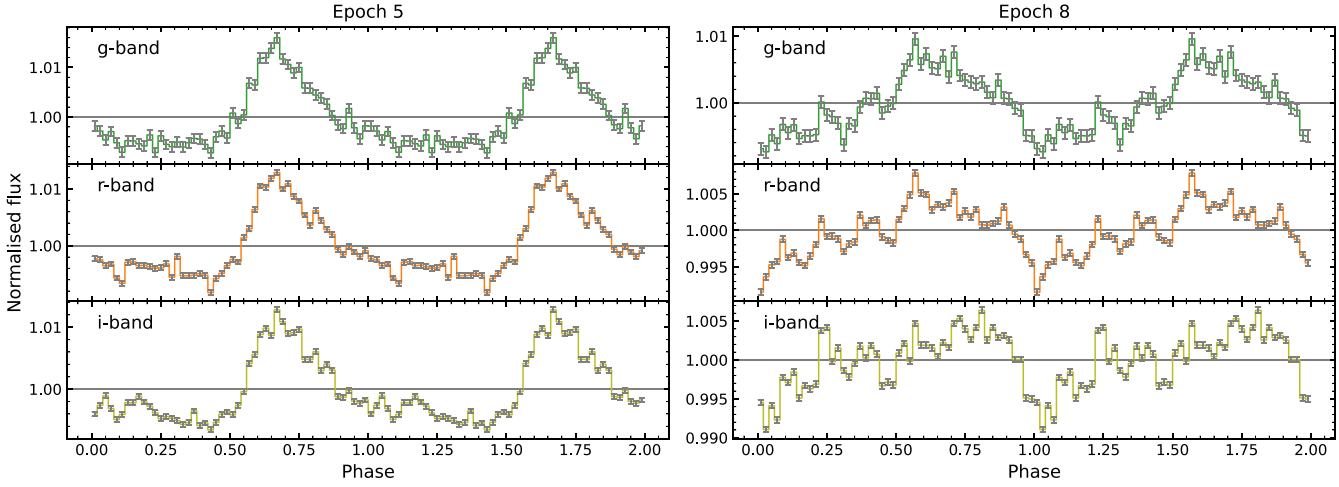

Figure A7. Light curves for Epochs 5 and 8 folded on the 317.91 s beat period.

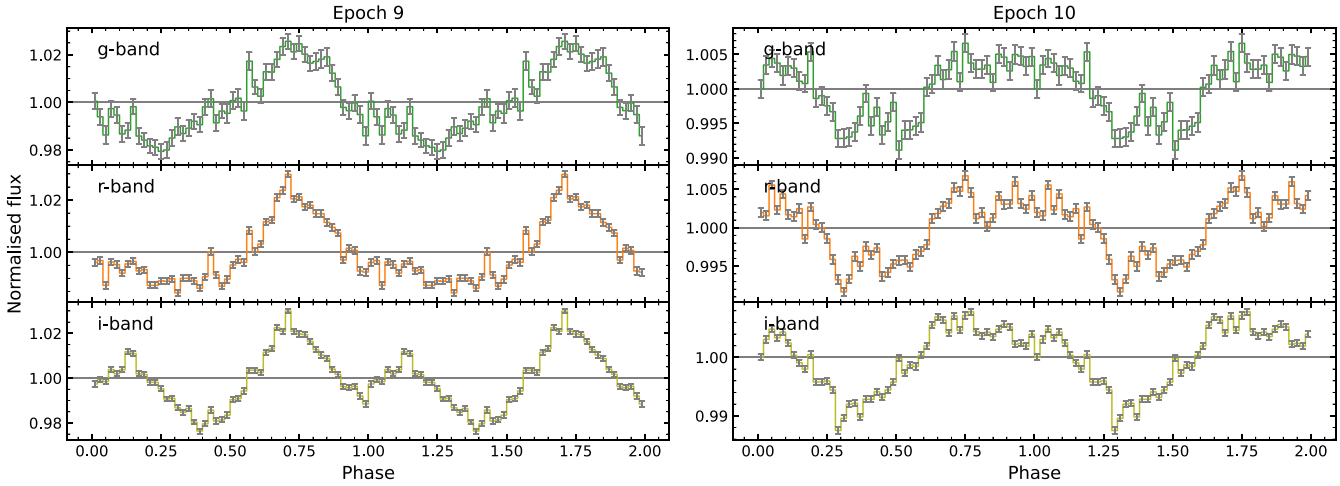

Figure A8. Light curves for Epochs 9 and 10 folded on the 317.91 s beat period.

This paper has been typeset from a TEX/LATEX file prepared by the author.